Electrical Power and Energy Systems 153 (2023) 109176

Contents lists available at ScienceDirect

International Journal of Electrical Power and Energy Systems

journal homepage: www.elsevier.com/locate/ijepes

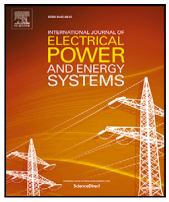

# Phase-leg power equalization method of modular multilevel converter with APOD strategy under unbalanced fault condition

Sang-Jung Lee [a,b], KiRyong Kim [a], Dae-Wook Kang [a], Jaesik Kang [a,*], Jee-Hoon Jung [b,*]

[a] Korea Electrotechnology Research Institute, 27, Dosicheomdansaneop-ro, Nam-gu, Gwangju, 61751, Gwangju, Republic of Korea
[b] Ulsan National Institute of Science and Technology, 50, UNIST-gil, Eonyang-eup, Ulju-gun, Ulsan, 44919, Ulsan, Republic of Korea

ARTICLE INFO

*Keywords:*
Modular multilevel converter (MMC)
Unbalanced grid fault
Imbalance control strategy
Power oscillation damping
Phase-leg power imbalance

ABSTRACT

An active power oscillation damping (APOD) control is one of the representative unbalanced fault compensation strategies. Recently, various studies have been performed on the effect of the APOD with the internal power dynamic analysis of a Modular Multilevel Converter (MMC); however, most of the papers have considered only the active power component for analyzing the internal dynamics of the MMC. During the APOD operation, while reactive power is supplied to the grid for the voltage compensation, phase-leg power imbalance can be aggravated. To enhance stability and reliability, the phase-leg power imbalance phenomenon should be sufficiently considered at the development stage of the controller. This research discovers that the phase-leg power imbalance rate could be determined by the magnitude and phase of the negative sequence component of the grid voltage and the amount of reactive power. In addition, the unbalanced power component can be accurately calculated only based on the grid voltage information and the reactive power reference. Also, this paper proposes a phase-leg power equalization method (PPEM) using unbalanced power component estimation. Furthermore, an improved control structure is also proposed to achieve more accurate phase-leg power equalization using the internal leg-energy dynamics analysis. The effectiveness of the proposed methods is verified through high-fidelity PSCAD/EMTDC time-domain simulations using Point-to-Point (PTP) MMC-HVDC system and Hardware-in-the-Loop Simulation (HILS) with the MMC-MVDC system.

## 1. Introduction

Modular multilevel converter (MMC) high-voltage direct current (HVDC) and flexible alternating current (AC) transmission systems (FACTS) are attracting global interest in the integration of various renewable energy sources [1–4]. Large-scale offshore wind or solar farms that supply bulk power to a specific region via HVDC transmission lines has a significant impact on grid stability when severe failure or shutdown on this backbone generation system occurs, which can cause serious problems and additional costs [5–7]. To minimize the aforementioned problem, a transmission system operator (TSO) recommends the continuous operation of a grid-connected power conversion system with grid support functions, such as low-voltage ride through, fault ride through, and reactive power compensation, even under grid fault conditions. Accordingly, enhanced MMC-HVDC and FACTS controls have become key technology for securing the stability and reliability of alternating/direct current (AC/DC) hybrid networks [8–15].

When an unbalanced fault occurs, imbalance voltage dip and swell cause overcurrent and oscillations of the dc-link voltage in the MMC–HVDC system. In the worst case, the MMC system is tripped by exceeding the rated capacity of the main components comprising the MMC system. Therefore, to ensure the required grid support in the case of grid failures, an imbalance control strategy that enables the stable operation of the MMC-HVDC system is essential [16–18]. A balanced positive-sequence control (BPSC) and an active power oscillation damping (APOD) are representative imbalance strategies. The BPSC injects only positive-sequence current components, even in asymmetric grid conditions, and the APOD can eliminate oscillation components in the active power and the dc-link voltage. Ref. [19] proposed an imbalance control method that can achieve the APOD or BPSC strategies by adjusting the proposed single coefficient. The proposed imbalance strategy has been validated in a four-leg inverter topology. Since those strategies are performed by controlling the current reference, they can be widely applied to various grid-connected power converters. However, the effect of the imbalance strategy on the internal electrical dynamics depends on the topology of the power converter. Therefore, it is required to analyze the effect of the imbalance strategy on the internal dynamics of the power converters, and the dynamics should be sufficiently reflected in the controller design for its stable operation. Ref. [20–24] analyzed the influence on the internal dynamics of the

* Corresponding authors.
*E-mail address:* jung.jeehoon@gmail.com (J.-H. Jung).

https://doi.org/10.1016/j.ijepes.2023.109176
Received 8 September 2022; Received in revised form 20 January 2023; Accepted 19 April 2023
Available online 7 June 2023

MMC topology in the imbalance strategy. In [20], the effects of the voltage dip factors and operating conditions on the arm current of the MMC have been studied under the BPSC strategy. This research indicates that the negative-sequence voltage component causes a DC component imbalance of the circulating current (CC), which increases the arm current of a specific phase.

In [21,22] the internal power dynamics of MMC have been analyzed in the APOD strategy. Unlike the BPSC strategy, the DC component of CC flowing in each phase is the same, so it is concluded that the phase-leg power is always balanced. Ref. [23] also proposed a circulating current suppression controller (CCSC) with a PIR structure that can balance the dc current of each phase while removing CC based on the assumption that the power of each phase is balanced in the APOD strategy. In [24], a comprehensive review of the operation and control methods applied to the MMC-HVDC system was performed with a specific focus on unbalanced grid conditions. This paper notices that the DC component of the CC of MMC is balanced under the APOD strategy, so the active power among the three phases is equal in the APOD strategy. It is well known that the phase-leg power is always the same in the APOD strategy. However, the above assumption is valid only when the power factor is unity at the MMC side. If the reactive power is simultaneously supplied to the grid, an unbalanced active power component can be generated by the current component corresponding to the reactive power. The unbalanced active power component does not change the total amount of active power, but it can generate a phase-leg power imbalance. However, no research has been conducted on the above phenomenon. If the controller is designed without considering the phase-leg power imbalance phenomenon, the MMC system stability is not guaranteed. As an example, since the CCSC proposed in [23] is designed under the assumption of phase-leg power balance, the dc current of each phase is equally controlled. Therefore, even when a phase-leg power imbalance occurs, the dc current of each phase is forcibly controlled equally. However, since the magnitude of the dc current is determined to balance the input/output power of the phase, the dc current cannot be used as a control variable to obtain phase-leg power equalization (PPE). If the dc current is forcibly controlled by ignoring the input and output power relationship, the sub-module capacitor voltage of a specific phase increases or decreases significantly. In the worst case, the MMC–HVDC system can be tripped due to exceeding the secured voltage range of the sub-module capacitor. Therefore, in order to simultaneously satisfy the requirements of TSO and the stability of the MMC system, the dynamic characteristics of the system must be reflected when designing the controller.

In this study, the effect of the reactive power components on the MMC internal power dynamics is analyzed comprehensively under the APOD strategy. In addition, based on the analysis of the MMC internal power dynamics, the phase-leg power equalization method (PPEM) based on the feed-forward structure is proposed to remove unbalanced power components in all the available PQ capability ranges. Since the feed-forward structure cannot eliminate steady-state errors caused by computation or measurement errors, precise PPE cannot be accomplished. Therefore, this paper also proposes an improved control structure based on internal leg-energy dynamics analysis to obtain precise PPE capability by minimizing the steady-state error caused by the feed-forward structure. Consequently, the control dynamics are improved, and precise power control can be achieved in various operating ranges without compromising the stability of the MMC-HVDC system under the APOD strategy. The proposed methods and analysis conducted in this paper are verified by high-fidelity PSCAD/EMTDC time-domain simulations and a Hardware-in-the-Loop Simulation (HILS) platform.

## 2. Imbalance control strategies based on instantaneous reactive power theory

For a three-phase system, the instantaneous active and reactive powers of the ac-side can be expressed as follows [25]:

$$p = \mathbf{v} \cdot \mathbf{i} = v_a i_a + v_b i_b + v_c i_c, \tag{1}$$

$$q = \mathbf{v}_\perp \cdot \mathbf{i} = \frac{1}{\sqrt{3}}(v_{a\perp} i_a + v_{b\perp} i_b + v_{c\perp} i_c). \tag{2}$$

where the bold symbols $\mathbf{v} = [v_a\ v_b\ v_c]^T$ and $\mathbf{i} = [i_a\ i_b\ i_c]^T$ denote the vector components and the subscript "$\perp$" is the orthogonal vector. When a voltage dip occurs during a single-phase to ground fault or phase-to-phase short circuit fault, the grid voltage and current may include not only a positive-sequence component but also zero-sequence and negative-sequence components. Typically, since zero-sequence voltages of unbalanced voltage dips do not exist in a three-phase system, nor can they propagate to the secondary side of star-ungrounded or delta-connected transformers, most case studies only consider the positive and negative sequences in the power analysis [19]. Based on the symmetric component method, the unbalanced components can be expressed as symmetrical positive- and negative-sequence components. Consequently, power equations (1) and (2) in the unbalanced condition can be re-expressed as follows:

$$p = \overbrace{\mathbf{v}^+ \cdot \mathbf{i}^+}^{P^+} + \overbrace{\mathbf{v}^- \cdot \mathbf{i}^-}^{P^-} + \overbrace{\mathbf{v}^+ \cdot \mathbf{i}^- + \mathbf{v}^- \cdot \mathbf{i}^+}^{\tilde{p}}, \tag{3}$$

$$q = \overbrace{\mathbf{v}_\perp^+ \cdot \mathbf{i}^+}^{Q^+} + \overbrace{\mathbf{v}_\perp^- \cdot \mathbf{i}^-}^{Q^-} + \overbrace{\mathbf{v}_\perp^+ \cdot \mathbf{i}^- + \mathbf{v}_\perp^- \cdot \mathbf{i}^+}^{\tilde{q}}, \tag{4}$$

where the superscripts + and − represent the positive- and negative-sequence components, and $P^{+,-}$, $Q^{+,-}$ and $\tilde{p}$, $\tilde{q}$ represent the constant and the oscillation terms, respectively. For independent active and reactive power control, the vector of the sequence current $\mathbf{i}^{+,-}$ can be divided into two orthogonal components $i_p^{+,-}$ and $i_q^{+,-}$, which have an in-phase relationship with $\mathbf{v}^{+,-}$ and $\mathbf{v}_\perp^{+,-}$, respectively. Based on (3) and (4), Ref. [19] proposed an imbalance control method that can achieve the APOD or BPSC strategies by adjusting the proposed single coefficient. Eq. (5) shows the current reference for the execution of the imbalance control strategy, and the detailed formula expansion is expressed in [19].

$$\begin{aligned}\mathbf{i}_{pq} = \mathbf{i}_p + \mathbf{i}_q = &\frac{P}{\|\mathbf{v}^+\|^2 + k_p\|\mathbf{v}^-\|^2}(\mathbf{v}^+ + k_p\mathbf{v}^-) \\ &+ \frac{Q}{\|\mathbf{v}^+\|^2 + k_q\|\mathbf{v}^-\|^2}(\mathbf{v}_\perp^+ + k_q\mathbf{v}_\perp^-)\end{aligned} \tag{5}$$

where operator "$\|\cdot\|$" means the norm of a vector, and the scalar coefficient $k_p$ and $k_q$ are the weighting factor. Coefficients $k_p$ and $k_q$ can be determined according to the imbalance control strategy. If the values of $k_p$ and $k_q$ are set to −1 and 0, the APOD and BPSC can be conducted, respectively. There are infinite combinations of the independent coefficients $k_p$ and $k_q$. In order to preserve controllability, the previous research of [19] has proposed two coefficient selection strategies in which $k_p$ and $k_q$ have the same sign ($k_p = k_q$) or opposite sign ($k_p = -k_q$) to simplify the link between the two coefficients. However, in the same sign strategy, the APOD strategy can be conducted only in the unity power factor condition. Therefore, the opposite sign strategy should be used to perform the APOD strategy in all the available PQ capability ranges [19]. In this paper, the MMC internal power dynamics in the APOD strategy based on the opposite sign strategy are also analyzed.

## 3. Power analysis for phase-leg power equalization

In this section, the internal power dynamics of the MMC are analyzed in the APOD strategy. For a clear interpretation, the power analysis proceeds based on some assumptions. First, the positive-sequence component of the ac-side voltage is always greater than that of the negative-sequence component under grid faults. Second, since a wye-wye or wye-delta transformer is generally employed between the ac-grid and the grid-connected converter, zero-sequence current can be excluded. Consequently, only positive- and negative sequence components exist on the secondary side of the transformer in both the line-to-line and phase-to-ground faults. Therefore, the power analysis

performed in this paper can be used in both the line-to-line and phase-to-ground faults. Finally, the power analysis is performed by an extensively used stationary reference frame.

Using the Clarke transform, three-phase voltage components can be expressed as $\alpha\beta$ components as follows:

$$\begin{bmatrix} v_\alpha^{+,-} \\ v_\beta^{+,-} \end{bmatrix} = \frac{1}{3}\begin{bmatrix} 2 & -1 & -1 \\ 0 & \sqrt{3} & -\sqrt{3} \end{bmatrix} \mathbf{v}^{+,-}. \tag{6}$$

Furthermore, the orthogonal components of the voltage vectors can be expressed as follows:

$$v_{\alpha\perp}^{+,-} = v_\beta^{+,-},\ v_{\beta\perp}^{+,-} = -v_\alpha^{+,-}. \tag{7}$$

The positive- and negative-sequence voltages can be defined as follows:

$$v_\alpha^+ = V^+\cos(\omega t + \varphi_v^+),\ v_\beta^+ = V^+\sin(\omega t + \varphi_v^+), \tag{8}$$

$$v_\alpha^- = V^-\cos(\omega t + \varphi_v^-),\ v_\beta^- = -V^-\sin(\omega t + \varphi_v^-), \tag{9}$$

where $\omega$ is the fundamental frequency and $V^{+,-}$ and $\varphi_v^{+,-}$ represent the magnitude and phase of the positive- and negative- sequence voltages, respectively. Based on (6) and (7), the constant and oscillation terms of active and reactive power components of (3) and (4) can be re-expressed as follows:

$$P = \frac{3}{2}[\overbrace{(v_\alpha^+ i_\alpha^+ + v_\beta^+ i_\beta^+)}^{P^+} + \overbrace{(v_\alpha^- i_\alpha^- + v_\beta^- i_\beta^-)}^{P^-}], \tag{10}$$

$$Q = \frac{3}{2}[\overbrace{(v_\beta^+ i_\alpha^+ - v_\alpha^+ i_\beta^+)}^{Q^+} + \overbrace{(v_\beta^- i_\alpha^- - v_\alpha^- i_\beta^-)}^{Q^-}], \tag{11}$$

$$\tilde{p} = \frac{3}{2}(v_\alpha^+ i_\alpha^- + v_\beta^+ i_\beta^- + v_\alpha^- i_\alpha^+ + v_\beta^- i_\beta^+), \tag{12}$$

$$\tilde{q} = \frac{3}{2}(-v_\alpha^+ i_\beta^- + v_\beta^+ i_\alpha^- - v_\alpha^- i_\beta^+ + v_\beta^- i_\alpha^+). \tag{13}$$

The constant active power term (10) is expressed as a product of the components of the same sequence with symmetry; the amount of output power from each phase is the same. According to the instantaneous reactive power theory, since the dot product between the different sequence components can be expressed in oscillation term (12) with zero mean values in three-phase power calculation, the amount of active power injected in the grid is determined by only (10). However, the average power of each phase caused by the oscillation term can be non-zero. Therefore, it is necessary to analyze the influence of the oscillation term on each phase-leg power. To analyze the effect of the reactive current component on each phase-leg power, the current reference including only the reactive current component and the weighting factor ($k_q$) can be expressed as follows using (5) and (7).

$$\mathbf{i}_q^+ = \mathbf{i}_{\alpha(q)}^+ + \mathbf{i}_{\beta(q)}^+ = \frac{Q}{\|\mathbf{v}_\alpha^+\|^2 + k_q\|\mathbf{v}_\alpha^-\|^2} v_\beta^+ - \frac{Q}{\|\mathbf{v}_\beta^+\|^2 + k_q\|\mathbf{v}_\beta^-\|^2} v_\alpha^+ \tag{14}$$

$$\mathbf{i}_q^- = \mathbf{i}_{\alpha(q)}^- + \mathbf{i}_{\beta(q)}^- = \frac{k_q Q}{\|\mathbf{v}_\alpha^+\|^2 + k_q\|\mathbf{v}_\alpha^-\|^2} v_\beta^- - \frac{k_q Q}{\|\mathbf{v}_\beta^+\|^2 + k_q\|\mathbf{v}_\beta^-\|^2} v_\alpha^- \tag{15}$$

By substituting (8) and (9) into (14) and (15), the reactive current component in the APOD strategy can be summarized as follows:

$$\mathbf{i}_q^+ = \mathbf{i}_{\alpha(q)}^+ + \mathbf{i}_{\beta(q)}^+ = I_q^+\sin(\omega t + \varphi_v^+) - I_q^+\cos(\omega t + \varphi_v^+), \tag{16}$$

$$\mathbf{i}_q^- = \mathbf{i}_{\alpha(q)}^- + \mathbf{i}_{\beta(q)}^- = -k_q[I_q^-\sin(\omega t + \varphi_v^-) + I_q^-\cos(\omega t + \varphi_v^-)], \tag{17}$$

where the magnitude of the current can be written as

$$I_q^{+,-} = \frac{QV^{+,-}}{\|\mathbf{v}_\alpha^+\|^2 + k_q\|\mathbf{v}_\alpha^-\|^2} = \frac{QV^{+,-}}{\|\mathbf{v}_\beta^+\|^2 + k_q\|\mathbf{v}_\beta^-\|^2}. \tag{18}$$

To analyze the effect of the reactive current component on the phase-leg power in the oscillation term, (12) can be re-expressed in (19).

$$\tilde{p} = \frac{3}{2}(\overbrace{v_\alpha^+ i_{\alpha(q)}^- + v_\alpha^- i_{\alpha(q)}^+}^{①} + \overbrace{v_\beta^+ i_{\beta(q)}^- + v_\beta^- i_{\beta(q)}^+}^{②}) \tag{19}$$

Eq. (20) shows the dot product result for the active power oscillation term (19).

$$\begin{aligned}
① &= -\frac{3V^+I_q^-k_q}{2}[\cos(\omega t + \varphi_v^+)\sin(\omega t + \varphi_v^-)] \\
&\quad + \frac{3V^-I_q^+}{2}[\cos(\omega t + \varphi_v^-)\sin(\omega t + \varphi_v^+)] \\
&= -\frac{3V^+I_q^-k_q}{4}[\sin(2\omega t + \varphi_v^+ + \varphi_v^-) - \sin(\varphi_v^+ - \varphi_v^-)] \\
&\quad + \frac{3V^-I_q^+}{4}[\sin(2\omega t + \varphi_v^+ - \varphi_v^-) - \sin(\varphi_v^- - \varphi_v^+)] \\
② &= -\frac{3V^+I_q^-k_q}{2}[\sin(\omega t + \varphi_v^+)\cos(\omega t + \varphi_v^-)] \\
&\quad + \frac{3V^-I_q^+}{2}[\sin(\omega t + \varphi_v^-)\cos(\omega t + \varphi_v^+)] \\
&= -\frac{3V^+I_q^-k_q}{4}[\sin(2\omega t + \varphi_v^+ + \varphi_v^-) + \sin(\varphi_v^+ - \varphi_v^-)] \\
&\quad + \frac{3V^-I_q^+}{4}[\sin(2\omega t + \varphi_v^+ + \varphi_v^-) + \sin(\varphi_v^- - \varphi_v^+)]
\end{aligned} \tag{20}$$

• Case 1 : With opposing-sign coefficients, ($k_q = 1$)

$$\begin{aligned}
① &= \frac{3V^+I_q^-}{4}[\sin(\varphi_v^+ - \varphi_v^-)] - \frac{3V^-I_q^+}{4}[\sin(\varphi_v^- - \varphi_v^+)] \\
&= \frac{3}{2}\frac{V^-V^+Q}{(V^+)^2 + (V^-)^2}\sin(\varphi_v^+ - \varphi_v^-) \\
② &= -\frac{3V^+I_q^-}{4}[\sin(\varphi_v^+ - \varphi_v^-)] + \frac{3V^-I_q^+}{4}[\sin(\varphi_v^- - \varphi_v^+)] \\
&= -\frac{3}{2}\frac{V^-V^+Q}{(V^+)^2 + (V^-)^2}\sin(\varphi_v^+ - \varphi_v^-)
\end{aligned}$$

• Case 2 : With same-sign coefficients, ($k_q = -1$)

$$① = -\frac{3V^+I_q^-}{4}[\sin(\varphi_v^+ - \varphi_v^-)] - \frac{3V^-I_q^+}{4}[\sin(\varphi_v^- - \varphi_v^+)] = 0$$

$$② = \frac{3V^+I_q^-}{4}[\sin(\varphi_v^+ - \varphi_v^-)] + \frac{3V^-I_q^+}{4}[\sin(\varphi_v^- - \varphi_v^+)] = 0$$

Note that the components $V^+I_q^-$ and $V^-I_q^+$ in (20) have the same magnitude, the dc terms in ① and ② can only be canceled or added according to the sign of the weighting factor. In the APOD strategy with the opposite sign strategy (Case 1 : $k_q$ is set to 1), the dc terms in ① and ② have an in-phase relationship and are added to each other. The dc terms redistributing the power of each phase may appear. This means that the reactive current component generates an unbalanced power component, indicating that the relationship between reactive power and active power is no longer independent in the APOD strategy. Since the sum of ① and ② is zero, the dc terms do not affect the amount of three-phase power. Therefore, the unbalanced power component is not observed in the three-phase power calculation. (In the same sign strategy (Case 2 : $k_q$ is set to −1), the dc terms of ① and ② cancel each other, unbalanced power component does not occur. However, the power oscillation is reproduced due to the reactive power current component [19].) The unbalanced power component can be expressed as an *abc* frame using the inverse Clarke transformation as follows:

$$\begin{aligned}
P_{un_a}^{+,-} &= \frac{3}{2}v_\alpha^{+,-}\cdot i_{\alpha(q)}^{-,+} \\
P_{un_b}^{+,-} &= \frac{3}{2}(\frac{1}{4}v_\alpha^{+,-}\cdot i_{\alpha(q)}^{-,+} - \frac{\sqrt{3}}{4}v_\beta^{+,-}\cdot i_{\alpha(q)}^{-,+} - \frac{\sqrt{3}}{4}v_\alpha^{+,-}\cdot i_{\beta(q)}^{-,+} + \frac{3}{4}v_\beta^{+,-}\cdot i_{\beta(q)}^{-,+}) \\
P_{un_c}^{+,-} &= \frac{3}{2}(\frac{1}{4}v_\alpha^{+,-}\cdot i_{\alpha(q)}^{-,+} + \frac{\sqrt{3}}{4}v_\beta^{+,-}\cdot i_{\alpha(q)}^{-,+} + \frac{\sqrt{3}}{4}v_\alpha^{+,-}\cdot i_{\beta(q)}^{-,+} + \frac{3}{4}v_\beta^{+,-}\cdot i_{\beta(q)}^{-,+})
\end{aligned} \tag{21}$$

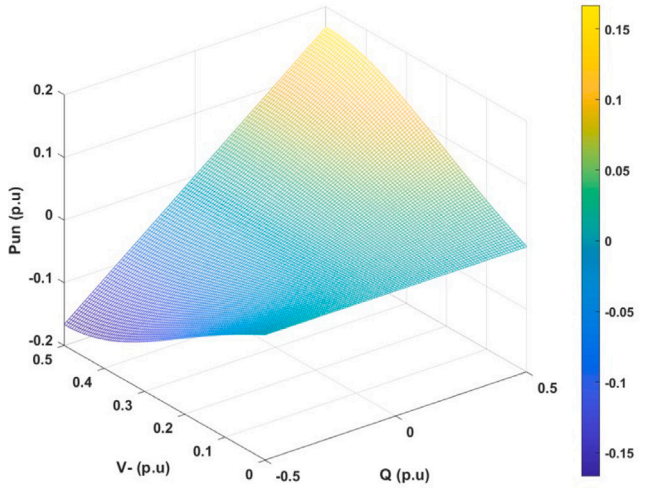


**Fig. 1.** Magnitude of the unbalanced power component generation trend according to $v^-$ and reactive power.

By substituting (8), (9), (16) and (17) into (21), the unbalanced power component can be expressed as

$$
\begin{aligned}
P_{un\_a} &= P_{un}\sin(\varphi_{v\_diff}) \\
P_{un\_b} &= \frac{\sqrt{3}P_{un}}{2}\cos(\varphi_{v\_diff}) - \frac{P_{un}}{2}\sin(\varphi_{v\_diff}) = P_{un}\sin(\varphi_{v\_diff} + \frac{2\pi}{3}) \\
P_{un\_c} &= -\frac{\sqrt{3}P_{un}}{2}\cos(\varphi_{v\_diff}) - \frac{P_{un}}{2}\sin(\varphi_{v\_diff}) = P_{un}\sin(\varphi_{v\_diff} - \frac{2\pi}{3}) \\
P_{un} &= \frac{3}{2}\frac{V^+V^-Q}{(V^+)^2 + (V^-)^2},\ \varphi_{v\_diff} = \varphi_v^+ - \varphi_v^-
\end{aligned}
\tag{22}
$$

where $P_{un}$ is the magnitude of the unbalanced power component and $\varphi_{v\_diff}$ is the phase difference between the positive and negative voltage sequence components of the ac-side voltage. Fig. 1 shows the magnitude of the unbalanced power component trend according to the negative-sequence voltage and reactive power. The unbalanced power component, $P_{un}$, is proportional to the reactive power and the magnitude of the negative-sequence voltage component. Therefore, as the reactive power and the negative sequence components increase, the power deviation between phases increases, which further exacerbates the phase-leg power imbalance phenomenon. The unbalanced power component has the characteristics that the direction rotates in the $a-c-b$ frame, and the power distribution is determined by the phase difference between the positive and negative voltage sequence components. As mentioned earlier, since the unbalanced power of each phase has a phase difference of 120°, the sum of the three-phase unbalanced power components is always zero. In summary, the assumption that the phase-leg power is always the same in the APOD strategy mentioned in [21–24] is valid only in the unity power factor.

In the MMC system, if dc-link is stiff and sub-module capacitor voltages are balanced because of the sorting method, the variation of the sub-module capacitor dc voltage is insignificant under phase-leg power imbalance conditions. However, the dc currents in the three phase-legs of MMC are unbalanced by the ac-side power. If the dc current components are forcibly readjusted without considering the input/output power balance of each phase as in [23] for PPE, a problem of increasing or decreasing the sub-module voltage occurs. In the worst case, the voltage of the sub-module is outside the normal operating range, and the MMC system trips. Therefore, a new control method is necessary to achieve PPE while performing the APOD strategy.

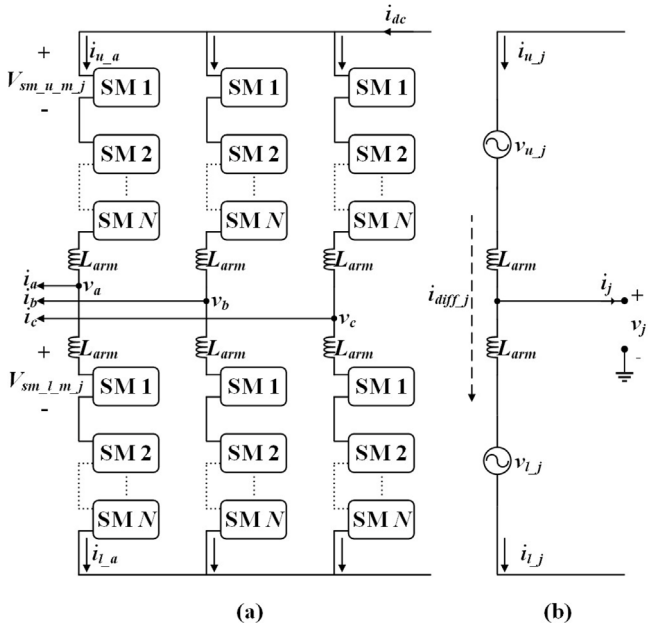


**Fig. 2.** Basic structure of MMC: (a) circuit diagram and (b) single-line equivalent circuit.

## 4. Proposed control method for phase-leg power equalization

### 4.1. Phase-leg power equalization method

In this section, the PPEM is proposed using a zero-sequence component voltage (ZV). Since the zero-sequence components have the same magnitude and phase in a three-phase system, its phase-leg power redistribution can be conducted without changing the total amount of power. Therefore, it is an appropriate control variable for the PPEM. Based on the unbalanced power calculated in (22), the equations used to achieve PPE using the ZV can be expressed as follows:

$$V_z\cos(\omega t + \varphi_z)\cdot I_a\cos(\omega t + \varphi_{i\_a}) + P_{un\_a} = 0, \tag{23}$$

$$V_z\cos(\omega t + \varphi_z)\cdot I_b\cos(\omega t + \varphi'_{i\_b}) + P_{un\_b} = 0. \tag{24}$$

where $V_z$ and $\varphi_z$ represent the voltage magnitude and the phase of the ZV, and $I_a$, $I_b$, and $\varphi_{i\_a}$, $\varphi'_{i\_b}$ represent the magnitude and phase of the ac current of phase-A and phase-B, respectively. Among the power components generated by the ZV, a dc component in which the second harmonic component is ignored can be expressed as follows:

$$\frac{V_zI_a}{2}\cos(\varphi_z - \varphi_{i\_a}) + P_{un\_a} = 0, \tag{25}$$

$$\frac{V_zI_b}{2}\cos(\varphi_z - \varphi'_{i\_b}) + P_{un\_b} = 0. \tag{26}$$

The magnitude of the ZV can be calculated by (27) according to phase-A or phase-B by combining (25) and (26).

$$
\begin{aligned}
V_z &= \frac{A}{\cos(\varphi_z - \varphi_{i\_a})}\ or\ \frac{B}{\cos(\varphi_z - \varphi'_{i\_b})} \\
A &= \frac{-2P_{un\_a}}{I_a},\ B = \frac{-2P_{un\_b}}{I_b},\ \varphi'_{i\_b} = \varphi_{i\_b} + \frac{2\pi}{3}
\end{aligned}
\tag{27}
$$

By rearranging (27) and using the trigonometric relationship, the phase of the ZV can be expressed as follows:

$$\varphi_z = \arctan\left\{\frac{A\cos(\varphi'_{i\_b}) - B\cos(\varphi_{i\_a})}{B\sin(\varphi_{i\_a}) - A\sin(\varphi'_{i\_b})}\right\} \tag{28}$$

where, $V_z$ for removing unbalanced power corresponding to phase-A or phase-B is calculated according to the coefficients $A$ and $B$, and $\varphi_z$

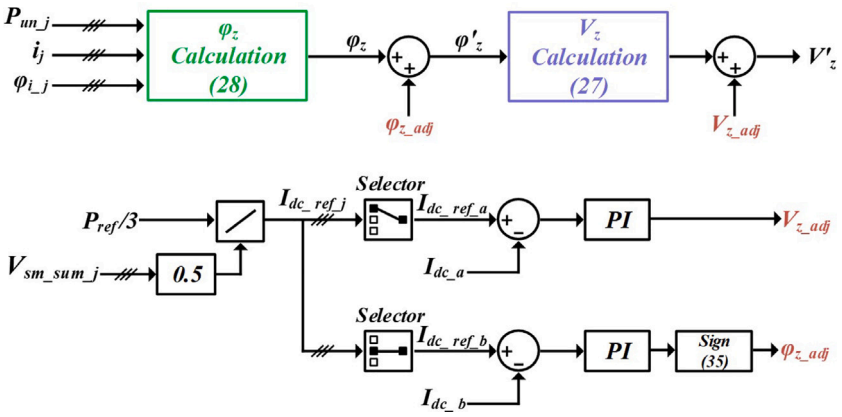


**Fig. 3.** Block diagram of the proposed enhanced phase-leg power equalization method (EPPEM).

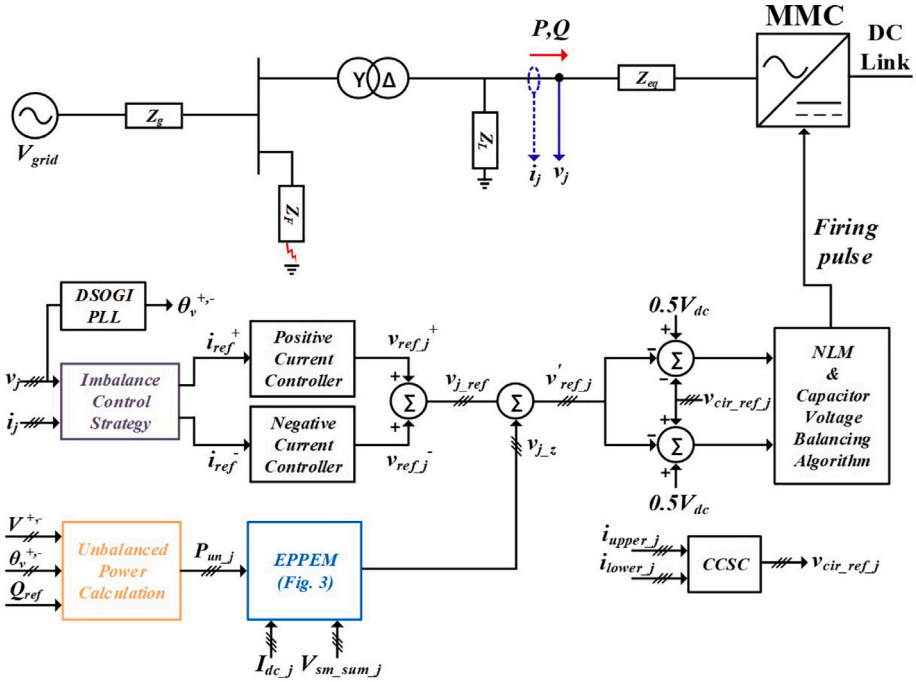


**Fig. 4.** Configuration diagram of MMC controller including the proposed EPPEM structure.

is calculated to simultaneously remove unbalanced power component of the remaining phases. PPE can be achieved by adding the ZV calculated by (27) and (28) to the reference voltage. Accurate magnitude and phase calculation of the ZV are required to obtain accurate PPE. However, obtaining the accurate voltage and current measurements are limited by the measurement error and delay of the sensor. Furthermore, because the PPEM has a feedforward structure, it cannot eliminate the steady-state error caused by the errors. Consequently, accurate PPE cannot be obtained only using the PPEM. In the next subsection, an efficient control structure is proposed to conduct precise PPE by minimizing the steady-state error.

### 4.2. Proposed enhanced phase-leg power equalization method

In the previous subsection, the PPEM was proposed based on the analysis of the ac-side power. In this subsection, the enhanced phase-leg power equalization method (EPPEM) is proposed with a closed-loop structure that can minimize the steady-state error using the dc-side power analysis on the MMC side. Fig. 2(a) and (b) show the circuit diagram of the MMC and the equivalent single-line circuit, respectively. The upper and lower arm currents of $i_{u\_j}$ and $i_{l\_j}$ can be expressed as follows:

$$i_{u\_j} = \frac{i_j}{2} + i_{diff\_j},\ i_{l\_j} = -\frac{i_j}{2} + i_{diff\_j},\ (j = a, b, c) \tag{29}$$

where $i_j$ is the ac-side current of each phase and $i_{diff\_j}$ is the CC. The CC consists of a dc component with even-order harmonic components as shown in (30).

$$i_{diff\_j} = I_{dc\_j} + \sum_{h=1}^{\infty} I_{diff\_h\_j} \sin(h\omega t - \varphi_{h\_j}) \tag{30}$$

In (30), $I_{dc\_j}$ corresponds to the power supplied from the dc-link, and $I_{diff\_h\_j}$ and $\varphi_{h\_j}$ are the amplitudes and phases of the harmonics, respectively. Assuming that the MMC–HVDC system is lossless, the amount of power supplied from the dc-link equals the output power supplied to the ac-side. Therefore, the phase-leg power relation

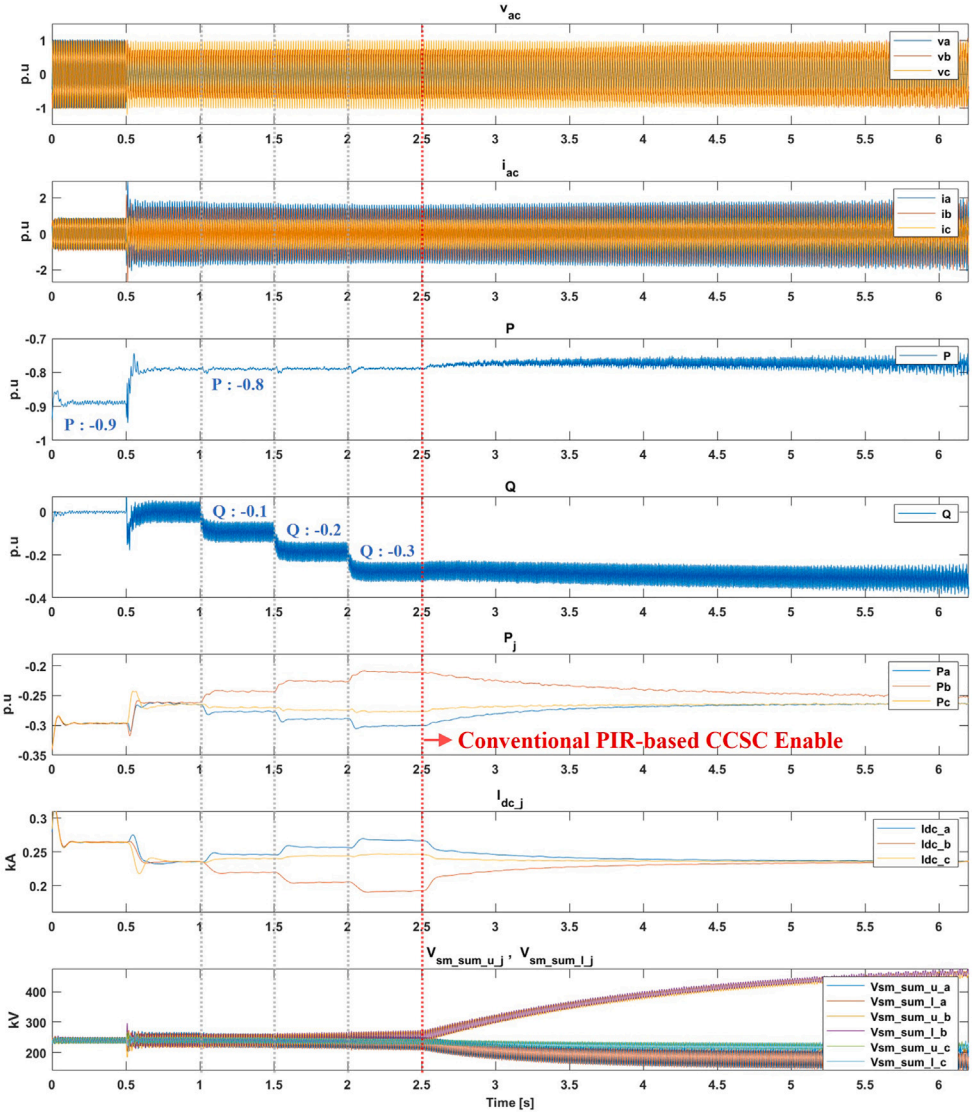


**Fig. 5.** Simulation results of the PPE using conventional PIR-based CCSC under APOD strategy; 0.5 [s] : the phase A-to-ground fault occurs; 0.5 [s] : the phase A-to-ground fault occurs, 1 [s] : reactive power begins to be supplied to the ac-side Q = −0.1 [p.u], 1.5 [s] : Q = −0.2 [p.u], 2 [s] : Q = −0.3 [p.u], 2.5 [s] : the PPE is performed using the conventional PIR-based CCSC [23].

between the ac-side and the dc-side can be expressed as follows:

$$P_{ac\_j} = P_{dc\_j} = v_j \cdot i_j = V_{sm\_sum\_j} \cdot I_{dc\_j}, \tag{31}$$

where $V_{sm\_sum\_j}$ is the average value of the sub-module voltages of the upper and lower arms and is expressed by (32).

$$V_{sm\_sum\_j} = \frac{1}{2}\sum_{m=1}^{N}(V_{sm\_u\_m\_j} + V_{sm\_l\_m\_j}) \tag{32}$$

Assuming that the power output to the ac-side in each phase is balanced, (31) is re-expressed as follows:

$$P_{ac\_avg} = P_{dc\_j} = V_{sm\_sum\_j} \cdot I_{dc\_j},\ P_{ac\_avg} = P_{ref}/3 \tag{33}$$

where $P_{ac\_avg}$ represents the average active power of each phase. Using (33), the dc current reference of each phase to conduct PPE can be expressed as (34).

$$I_{dc\_ref\_j} = \frac{P_{ac\_avg}}{V_{sm\_sum\_j}} \tag{34}$$

Because the dc value has fewer measurements and calculation errors compared with the ac value, it can be used as a more accurate reference. By adjusting the dc current of each phase based on (34), $V_z$ and $\varphi_z$ calculated by the ac-side power analysis can be re-adjusted to achieve accurate PPE. In (27), one of the coefficients $A$ and $B$ can be used to calculate $V_z$. If coefficient A is used, $V_z$ is calculated to remove $P_{un\_a}$. Therefore, $I_{dc\_ref\_a}$ can be used to adjust $V_z$, and $I_{dc\_ref\_b}$ or $I_{dc\_ref\_c}$ can be used as reference to adjust $\varphi_z$. When adjusting $\varphi_z$, it is necessary to define the sign to adjust the magnitude of the dc current based on the initial value of $\varphi_z$. Eq. (35) shows the sign definition of $\varphi_{z\_adj}$ according to the initial value of $\varphi_z$ and the magnitude of the dc current based on (25) and (26).

$$\varphi_{z\_adj} = \begin{cases} +\varphi_{z\_adj}, \text{ if } \|I_{dc\_ref\_j}\| < \|I_{dc\_j}\|,\ 0 < \varphi_z < \frac{\pi}{2} \\ -\varphi_{z\_adj}, \text{ if } \|I_{dc\_ref\_j}\| > \|I_{dc\_j}\|,\ 0 < \varphi_z < \frac{\pi}{2} \\ -\varphi_{z\_adj}, \text{ if } \|I_{dc\_ref\_j}\| < \|I_{dc\_j}\|,\ \frac{\pi}{2} < \varphi_z < \pi \\ +\varphi_{z\_adj}, \text{ if } \|I_{dc\_ref\_j}\| > \|I_{dc\_j}\|,\ \frac{\pi}{2} < \varphi_z < \pi \end{cases} \tag{35}$$

Fig. 3 shows the proposed EPPEM with a closed-loop control structure. Based on the average value of active power and the average value of the sub-module voltages of each phase, the dc current reference that can achieve PPE can be calculated. $I_{dc\_ref\_a}$ is selected for $V_z$ adjustment by the selector according to the coefficient $A$ used for calculating $V_z$. The difference between the measured dc current and the calculated current reference is the input of the PI controller, and the output $V_{z\_adj}$

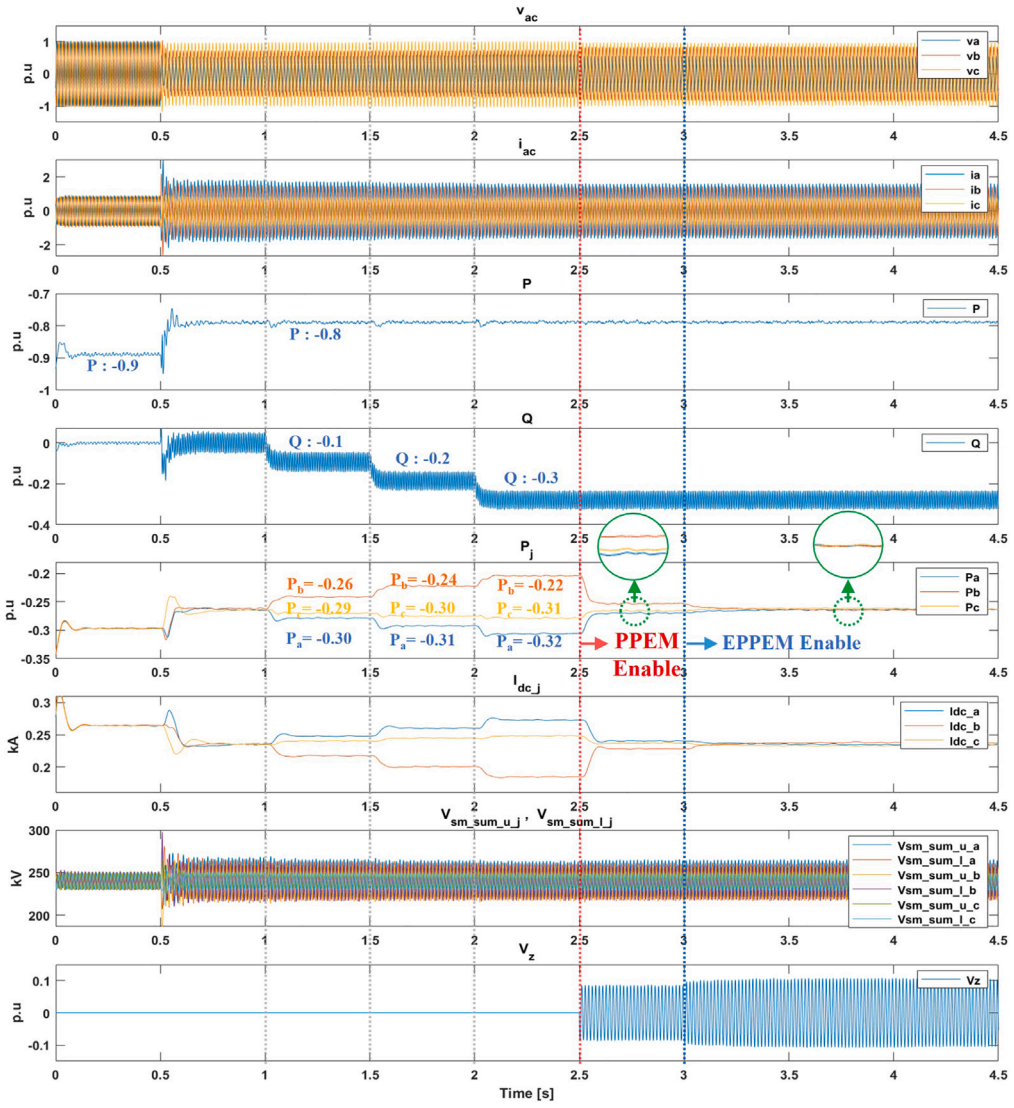


**Fig. 6.** Simulation results of the PPE using proposed PPEM and EPPEM under APOD strategy; 0.5 [s] : the phase A-to-ground fault occurs; 0.5 [s] : the phase A-to-ground fault occurs, 1 [s] : reactive power begins to be supplied to the ac-side Q = −0.1 [p.u], 1.5 [s] : Q = −0.2 [p.u], 2 [s] : Q = −0.3 [p.u], 2.5 [s] : PPEM enable, 3 [s] : EPPEM enable.

is added to the calculation result of (27). For adjusting $\varphi_z$, $I_{dc\_ref\_b}$ is selected through the selector, and the difference between the measured dc current and the calculated dc current reference is the input of the PI controller. The sign of the output $\varphi_{z\_adj}$ is determined by (35). Finally, $\varphi_{z\_adj}$ is added to the calculation result of (28). As a result, both the phase and the magnitude of the ZV can be re-adjusted by the proposed EPPEM. Hence, it is possible to conduct accurate phase-leg power control by eliminating the steady-state error.

## 5. Software-based simulation results

In this section, the analysis of the unbalanced power generation trend and the performance of the proposed methods are verified by PSCAD/EMTDC simulation tools using a 200 MW MMC–HVDC model. Table 1 lists the system parameters of the 200 MW MMC station. Fig. 4 shows the control structure of the imbalance control strategy widely used in MMC with the proposed control block. The sequence decomposition of voltage and current can be performed by the double second-order generalized integrator for quadrature-signals generation (DSOGI-QSG) method. The positive and negative sequence current reference for the APOD strategy is calculated in imbalance control strategy block based on (5), and the voltage reference can be obtained by each sequence current controller. The ZV that can conduct precise PPE is calculated by the unbalanced power calculation block and the proposed EPPEM block, and it is added to the voltage reference. Fig. 5 shows the simulation waveforms of the APOD strategy with the CCSC proposed in [23] under several scenario conditions. The simulation

**Table 1**
System parameters for the 200 MW multilevel converter–high-voltage-direct-current system.

| Parameters | Value |
|---|---|
| AC grid voltage (L-L, RMS), $V_{ac}$ | 154 [kV] |
| Frequency, $f_o$ | 60 [Hz] |
| AC system inductance, $L_s$ | 10 [mH] |
| Transformer winding voltage (L-L, RMS) | 154 [kV]/116.7 [kV] |
| Direct current (DC)-link voltage, $V_{dc}$ | ±120 [kV] |
| Rated active power, $P$ | 200 [MW] |
| Rated reactive power, $Q$ | 100 [VAR] |
| Sub-module capacitor, $C_{sm}$ | 6900 [uF] |
| Number of sub-modules per arm, $N$ | 100 [EA] |
| Voltage of sub-module capacitor, $V_{sm}$ | 2.4 [kV] |
| Arm inductance, $L_{arm}$ | 20 [mH] |

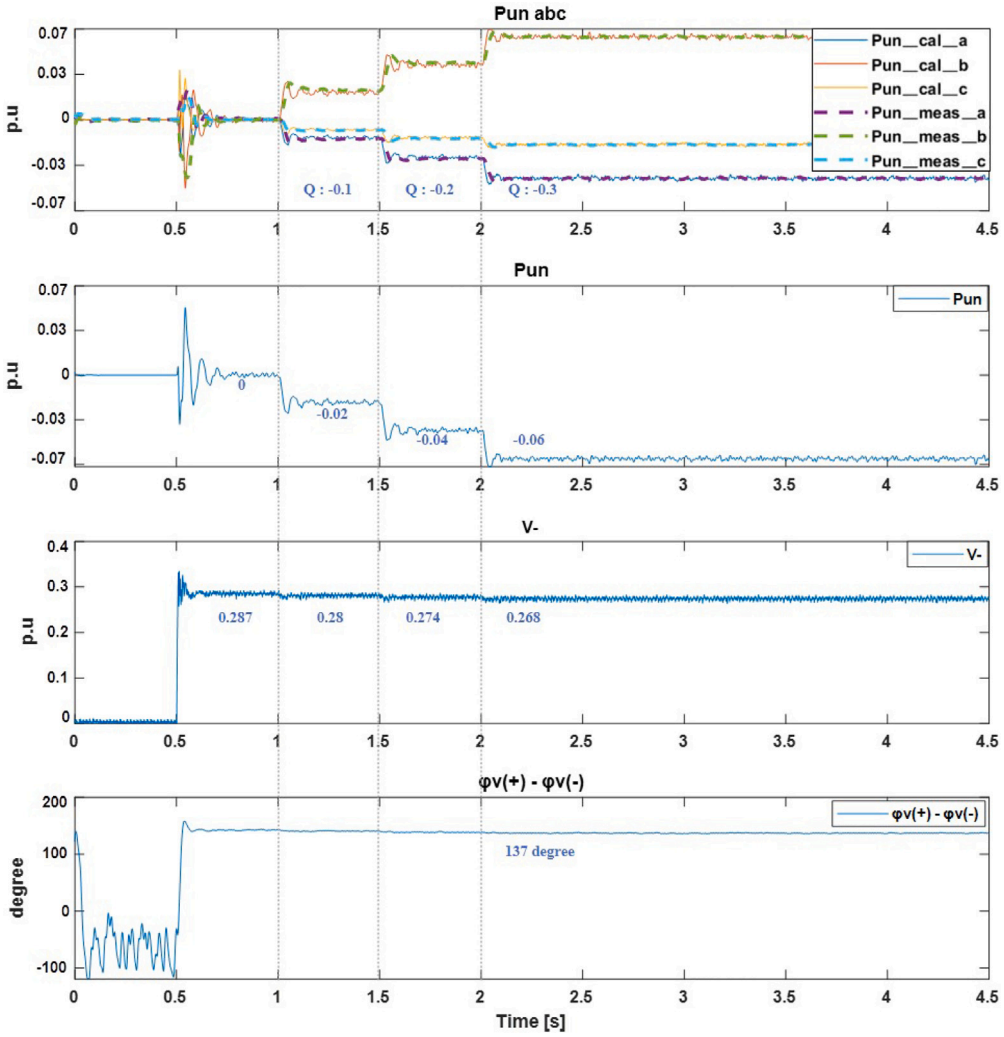


**Fig. 7.** Comparison of numerical analysis and simulation results of the unbalanced power components.

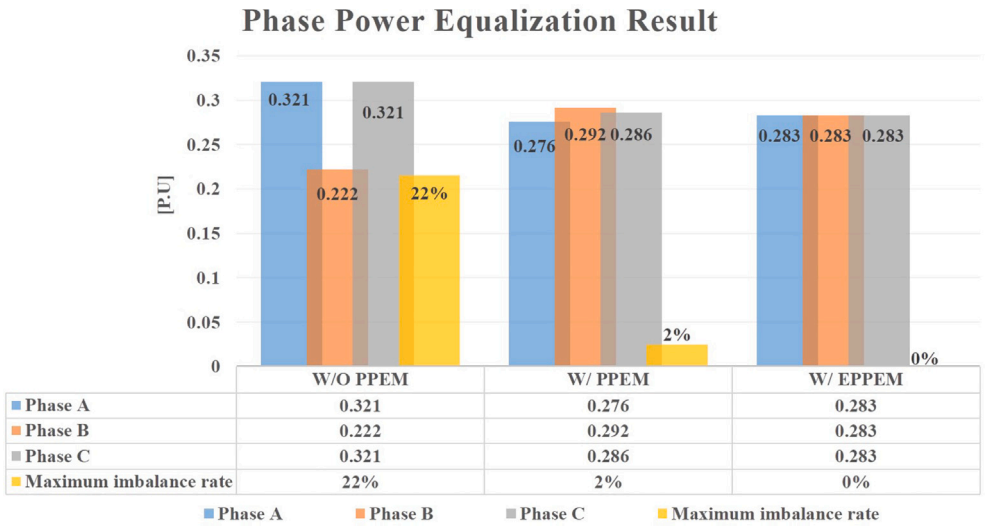


**Fig. 8.** Phase-leg power equalization results according to alternative control methods.

scenarios are as follows: The MMC operates at P = −0.9 [p.u] and Q = 0 [p.u] in a normal grid condition (0 < t < 0.5 s). After 0.5 s, phase A-to-ground fault occurs, and the APOD strategy is performed simultaneously. At this time, the active power is reduced to −0.8 [p.u] to protect the sub-module components. It can be observed that the second-harmonic power oscillation can be canceled even in the grid

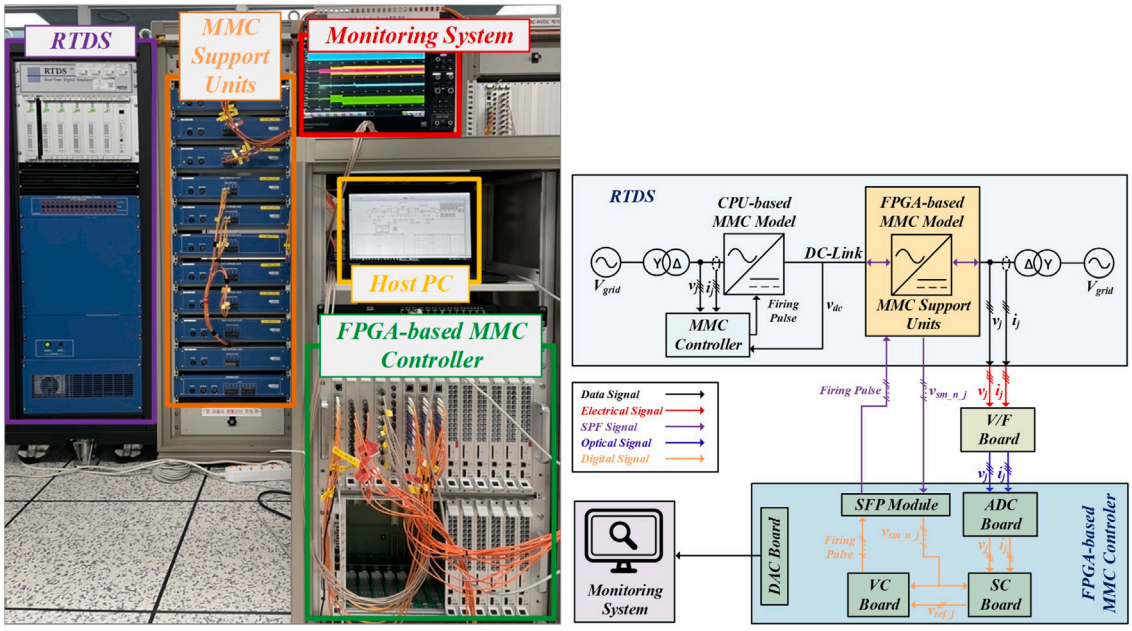


(a) (b)

**Fig. 9.** HILS setupts: (a) 30 MW PTP MMC system HILS test platform structure, (b) HILS test platform for 30 MW PTP MMC system.

**Table 2**
Comparison of controllability according to control method.

| Description | | Control method | | |
|---|---|---|---|---|
| | | Same-sign coefficient | Opposite-sign coefficient | Opposite-sign coefficient with EPPEM |
| APOD | $\tilde{p}$ elimination | Yes | Yes | Yes |
| Without Q | PPE | Yes | Yes | Yes |
| APOD | $\tilde{p}$ elimination | No | Yes | Yes |
| With Q | PPE | Yes | No | Yes |

fault condition. Since only active power is supplied to the ac-side, a phase-leg power imbalance phenomenon does not appear. The reactive power is supplied to the grid by 0.1 [p.u], 0.2 [p.u], and 0.3 [p.u] at 1 [s], 1.5 [s], and 2 [s], respectively. Since the unbalanced power component is generated by reactive power from 1 [s], each phase-leg power begins to be redistributed. From 2.5 [s] onward, the PPE is performed by the CCSC proposed in Ref. [23]. Although the dc current of each phase is balanced by the CCSC, the voltage of the sub-module capacitor is increased or decreased because the dc current is forcibly controlled without considering the input/output power balance of the phases. In the worst case, the MMC system is tripped because the capacitor voltage of sub-module may go out of operating range.

Fig. 6 shows the simulation waveforms of the APOD strategy including the proposed methods under the same scenario conditions. After 1 [s], the unbalanced power component generated by reactive power, each phase-leg power begins to be redistributed. In this case, each phase-leg power is approximately −0.30 [p.u], −0.26 [p.u] and −0.29 [p.u], respectively. After 1.5 [s], the reactive power supply increases to −0.2 [p.u], and each phase-leg power is −0.31 [p.u], −0.24 [p.u] and −0.3 [p.u]. Finally, from 2 [s] onward, reactive power increases by −0.3 [p.u], each phase-leg power is −0.32 [p.u], −0.22 [p.u] and −0.31 [p.u], respectively. According to the simulation results, it can be confirmed that reactive power causes the phase-leg power imbalance. As reactive power increases, the phase-leg power imbalance phenomenon becomes more severe. Fig. 7 shows a comparison of the numerical analysis and simulation results of the unbalanced power generation trends. The simulation scenario is the same as before, and its numerical analysis result can be obtained by (22). In Fig. 7, from the top, the unbalanced power components of each phase, the magnitude of the unbalanced power component ($P_{un}$), the magnitude of the negative-sequence voltage, and the phase difference between the positive- and negative-sequence voltages are illustrated. The power of $P_{un\_cal\_j}$ is the calculated value based on theoretical analysis, and $P_{un\_meas\_j}$ is the measured value. It is obvious that the numerical analysis results and simulation results have similar outcomes. From 2.5 [s] onward, the PPEM is enabled. PPE can be achieved by redistributing only the unbalanced power component. However, precise PPE cannot be conducted owing to steady-state errors. From 3 [s] onward, the proposed EPPEM is enabled. Both the phase and magnitude of the ZV are re-adjusted by $V_{z\_adj}$ and $\varphi_{z\_adj}$ based on the dc-side power analysis. As a result, precise PPE can be conducted by minimizing the steady-state error.

The main aspects of the control method are listed in Table 2. The same sign coefficient strategy always achieves the PPE. However, the APOD can be conducted only in the unity power factor condition. Conversely, the opposite sign coefficient strategy can achieve the APOD at various operating points of PQ capability. The phase-leg power imbalance occurs when power factor is not unity. By using the EPPEM, accurate PPE can be conducted without compromising the performance of the APOD strategy. Fig. 8 shows the performance comparison of the proposed method at the operating conditions of P = −0.9 [p.u] and Q = −0.3 [p.u]. Without the PPEM, the maximum imbalance rate is approximately 20% (0.1 [p.u]). When the PPEM is applied, PPE is almost done; however, there is approximately 2% (0.08 [p.u]) unbalanced power caused by the steady-state error. With the proposed EPPEM, precise PPE with zero unbalance rate can be conducted.

## 6. Hardware-in-the-loop simulation results

In this section, the proposed method is verified on a hardware-in-the-loop simulation (HILS) test platform shown in Fig. 9(a). The

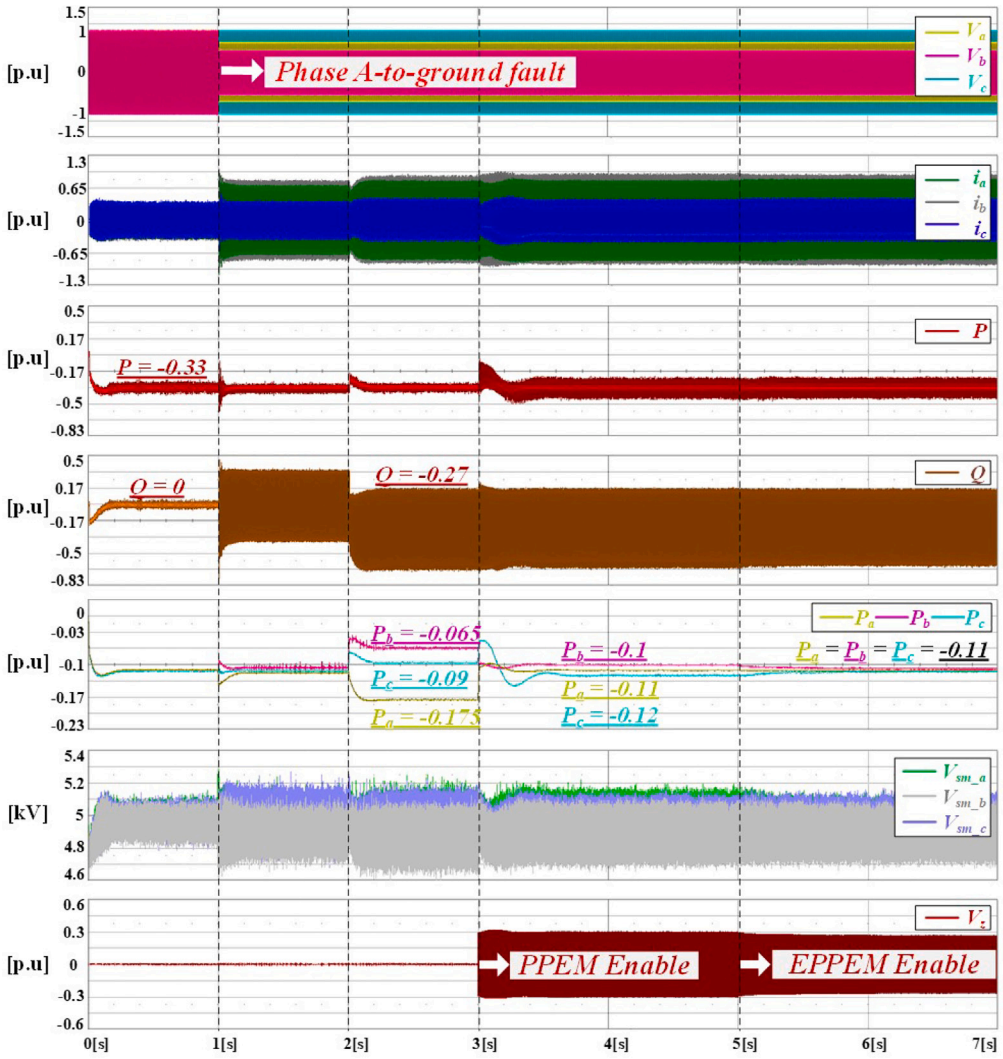


**Fig. 10.** Simulation waveforms of the HILS test results; 1 [s]: the phase A-to-ground fault occurs, 2 [s]: reactive power begins to be supplied to the AC side Q = −0.27 [p.u], 3 [s]: PPEM enable, 5 [s]: EPPEM enable.

**Table 3**
MMC system parameters for HILS.

| Parameters | Value |
|---|---|
| AC grid voltage (L-L, RMS), $V_{ac}$ | 22.9 [kV] |
| Frequency, $f_o$ AC system inductance, $L_s$ | 60 [Hz] |
| | 1 [mH] |
| Transformer winding voltage (L-L, RMS) | 22.9 [kV]/15.94 [kV] |
| Direct current (DC)-link voltage, $V_{dc}$ | ±15 [kV] |
| Rated active power, $P$ | 30 [MW] |
| Rated reactive power, $Q$ | 15 [VAR] |
| Sub-module capacitor, $C_{sm}$ | 5800 [uF] |
| Number of sub-modules per arm, $N$ | 12 [EA] |
| Voltage of sub-module capacitor, $V_{sm}$ | 2.5 [kV] |
| Arm inductance, $L_{arm}$ | 8 [mH] |

detailed structure of the HILS test platform is depicted in Fig. 9(b). This structure includes: (a) RTDS simulator that calculates CPU-based MMC model and ac-side grid; (b) MMC support units that calculate the MMC model at the FPGA level based on firing pulse signals transmitted from an external controller; (c) a field-programmable gate array (FPGA)-based MMC controller; (d) a voltage to frequency (V/F) converter board for transmitting electrical data for the MMC control from the RTDS simulator to the MMC controller. The MMC controller is implemented on the Xilinx Virtex-7 FPGA, which consists of an Analog-to-Digital Converter (ADC) board, a Digital-to-Analog Converter (DAC) board, a Supervisor Controller (SC) board, and a Valve Controller (VC) board. The SC corresponds to a high-level controller and calculates the voltage reference based on electrical data received from the ADC board. Based on the voltage reference received from the SC board, the VC board corresponds to a low-level controller, and calculates capacitor voltage balancing and the nearest level modulation (NLM) algorithm. The output signal of the VC board is the firing pulse signal transmitted to the MMC support units via the SPF module. The key waveform of the HILS test is the output of the DAC, which is monitored by a high-definition oscilloscope (WaveRunner 8000HD model). The HILS test platform was developed for a 30 MW point-to-point (PTP) MMC system. Table 3 presents the specifications of the MMC system. The basic operation of the PTP MMC system is as follows: the CPU-based MMC model operates in a rectifier mode, and the FPGA-based MMC model is operates in an inverter mode. The grid fault scenario assumes that a single-phase ground fault occurs on the FPGA-based MMC side. Fig. 10 shows key waveforms of HILS test results (from top to bottom), ac-side voltage, output current, the active and reactive power output from the MMC side, the output power of each phase, the average voltage of the sub-module of each phase, and the ZV. The simulation scenario is as follows: The FPGA-based MMC operates at P = 0.33 [p.u] and Q = 0 [p.u] at the normal grid condition (0 < t < 1 [s]). After 1 [s], the phase A-to-ground fault (voltage dip factor: 0.3 [p.u]) occurs, and the APOD

strategy with the opposite sign coefficient is performed simultaneously. After 2 [s], reactive power is supplied to the grid at approximately −0.27 [p.u] and each phase-leg power is −0.175 [p.u], −0.065 [p.u] and −0.09 [p.u]. From 3 [s] onward, the PPEM is applied to begin PPE. In this case, each phase-leg power is −0.11 [p.u], −0.1 [p.u] and −0.12 [p.u], respectively, and the maximum imbalance rate is approximately 9%. The proposed EPPEM is enabled at 5 [s], and precise PPE can be conducted by the proposed closed-loop control structure. In this case, the maximum phase-leg power imbalance rate is reduced from 9% to 0%.

## 7. Conclusion

In this paper, the tendency of the phase-leg power imbalance according to reactive power and voltage dip factor is analyzed under the APOD strategy. Based on the ac-side power analysis, the PPEM with the feed-forward structure is proposed to obtain PPE and improve the power dynamics of the MMC system. In addition, for more accurate PPE, the EPPEM based on the closed-loop structure, which can minimize the steady-state errors, is also proposed by the dc-side power analysis of the MMC side. The effectiveness of the proposed methods is verified through high-fidelity PSCAD/EMTDC time-domain simulations and the HILS test platform. The software-based simulation and HILS results indicate that, when the PPEM is used, PPE is obtained with an error of approximately 2%. With EPPEM, precise PPE with zero unbalance rate can be achieved. There are limitations of the method proposed in this paper. The over-modulation phenomenon can occur by zero-sequence voltage injection by proposed method. Over-modulation may cause a phenomenon in which the PQ operation area is reduced, and conversely, the PPE may be restricted under the condition of maintaining the PQ operation area. This is a limitation of the proposed method. Therefore, further research is needed on the optimal control method considering grid fault rate, PQ operation area, and phase-leg power imbalance rate.

## Declaration of competing interest

The authors declare that they have no known competing financial interests or personal relationships that could have appeared to influence the work reported in this paper.

## Data availability

Data will be made available on request

## References

[1] Debnath S, Saeedifard M. A new hybrid modular multilevel converter for grid connection of large wind turbines. IEEE Trans Sustain Energy 2013;4(4):1051–64.
[2] Nami A, Liang J, Dijkhuizen F, Demetriades GD. Modular multilevel converters for HVDC applications: Review on converter cells and functionalities. IEEE Trans Power Electron 2015;30(1):18–36.
[3] P HM, Bina MT. A transformerless medium-voltage STATCOM topology based on extended modular multilevel converters. IEEE Trans Power Electron 2011;26(5):1534–45.
[4] Antonopoulos A, Angquist L, Nee H. On dynamics and voltage control of the modular multilevel converter. In: 13th Eur. conf. power electron. appl. 2009, p. 1–10.
[5] Timofejevs A, Gamboa D, Liserre M, Teodorescu R, Chaudhary SK. Control of transformerless MMC-HVDC during asymmetric grid faults. In: IECON 2013-39th ann. conf. ieee ind. electron. soc. 2013, p. 2016–21.
[6] Maia de Sousa GJ, Da Silva Dias A, Alves JA, Heldwein ML. Modeling and control of a modular multilevel converter for medium voltage drives rectifier applications. In: 2015 IEEE 24th int. symp. ind. electron.. ISIE, 2015, p. 1080–7.
[7] Marzoughi A, Burgos R, Boroyevich D. Optimum design guidelines for the modular multilevel converter in active front-end applications: Considerations for passive component reduction. IEEE Power Electron Mag 2018;5(2):56–65.
[8] Son GT, et al. Design and control of a modular multilevel HVDC converter with redundant power modules for non-interruptible energy transfer. IEEE Trans Power Deliv 2012;27(3):1611–9.
[9] Altin M, et al. Overview of recent grid codes for wind power integration. In: Proc. 12th int. conf. optim. elect. electron. equip. 2010, p. 1152–60.
[10] Martin-Martinez S, et al. Participation of wind power plants in the spanish power system during events. In: Proc. IEEE power energy soc. gen. meet. 2012, p. 1–8.
[11] Li K, Yuan L, Zhao Z, Lu S, Zhang Y. Fault-tolerant control of MMC with hot reserved submodules based on carrier phase shift modulation. IEEE Trans Power Electron 2017;32(9):6778–91.
[12] Yang S, Tang Y, Wang P. Seamless fault-tolerant operation of a modular multilevel converter with switch open-circuit fault diagnosis in a distributed control architecture. IEEE Trans Power Electron 2018;33(8):7058–70.
[13] Leon AE, Amodeo SJ. Energy balancing improvement of modular multilevel converters under unbalanced grid conditions. IEEE Trans Power Electron 2017;32(8):6628–37.
[14] Shi X, Wang Z, Liu B, Liu Y, Tolbert LM, Wang F. Characteristic investigation and control of a MMC-based HVDC system under single-line-to-ground fault conditions. IEEE Trans Power Electron 2015;30(1):408–21.
[15] Judge P, Green T. Dynamic thermal rating of a modular multilevel converter HVDC link with overload capacity. In: Proc. IEEE eindhoven power tech. 2015, p. 1–6.
[16] Tu Q, Xu Z, Chang Y, Guan L. Suppressing DC voltage ripples of MMC-HVDC under unbalanced grid conditions. IEEE Trans Power Deliv 2012;27(3):1332–8.
[17] Bordignon P, Marchesoni M, Parodi G, Vaccaro L. Modular multilevel converter in HVDC systems under fault conditions. In: Proc.IEEE 15th Eur. conf. power electron. appl. sep. 2013, p. 1–10.
[18] Guo C, Yang J, Zhao C. Investigation of small-signal dynamics of modular multilevel converter under unbalanced grid conditions. IEEE Trans Ind Electron 2019;66(3):2269–79.
[19] Wang F, Duarte JL, Hendrix MAM. Pliant active and reactive power control for grid-interactive converters under unbalanced voltage dips. IEEE Trans Power Electron 2011;26(5):1511–21.
[20] Wang J, Tang Y, Liu X. Arm current balancing control for modular multilevel converters under unbalanced grid conditions. IEEE Trans Power Electron 2020;35(3):2467–79.
[21] Vasiladiotis M, Cherix N, Siemaszko D, Rufer A. Operation of modular multilevel converters under grid asymmetries. In: IECON 2013-39th annual conference of the IEEE industrial electronics society, 2013. 2013, p. 6281–6.
[22] Do W-S, Kim S-H, Kim T-J, Kim R-Y. A study of circulating current in MMC based HVDC system under an unbalanced grid condition. In: IECON 2014-40th annual conference of the IEEE industrial electronics society. 2014, p. 4146–52.
[23] Moon J, Kim C, Park J, Kang D, Kim J. Circulating current control in MMC under the unbalanced voltage. IEEE Trans Power Deliv 2013;28(3):1952–9.
[24] Li J, Konstantinou G, Wickramasinghe HR, Pou J. Operation and control methods of modular multilevel converters in unbalanced ac grids: A review. IEEE Trans Emerg Sel Top Power Electron 2019;7(2):1258–71.
[25] Akagi H, Watanabe EH, Aredes M. Instantaneous Power Theory and Applications To Power Conditioning. IEEE Press; 2007.